JOURNAL OF SPACECRAFT AND ROCKETS
Vol. 38, No. 3, May–June 2001

Experimental Investigations and Numerical Modeling of Pulsed Plasma Thruster Plumes

Nikolaos A. Gatsonis,* Robert Eckman,† and Xuemin Yin‡
Worcester Polytechnic Institute, Worcester, Massachusetts 01609
and
Eric J. Pencil,§ and Roger M. Myers¶
NASA John H. Glenn Research Center at Lewis Field, Cleveland, Ohio 44135

Integration of pulsed plasma thruster (PPT) onboard spacecraft requires the evaluation of potential plume/spacecraft interactions. Important findings are summarized of our experimental and modeling plume investigations of rectangular-geometry Teflon® PPTs. Initial studies of the Lincoln Experimental Satellite 8/9 PPT plume used time-of-flight analysis of single langmuir probe data and found two ion populations with approximately 30 and 60 km/s, respectively. A residual gas analyzer identified C, F, C_xF_y, and various thruster materials. Fast ionization gauges detected the presence of slow neutral particles up to 1 ms after the end of the discharge. Subsequent studies used triple langmuir probes and obtained electron temperature and density in the plume of a laboratory PPT operating at 5, 20, and 40 J. Plume properties showed large angular density variation on the perpendicular to the electrodes plane but small variation on the parallel plane. Electron density and temperature were found to decrease with increasing radial distance from the Teflon surface. Time-average temperatures were between 1 and 3 eV. Time-average electron density increased with increasing discharge energy and are in the range between 10^{19} and 2×10^{20} m^{-3} for 5 J, 6×10^{20} to 10^{21} m^{-3} for 20 J, and 2×10^{20} to 1.4×10^{21} m^{-3} for 40 J. The PPT plume model is based on a hybrid (particle–fluid) methodology. Neutrals and ions were modeled with a combination of the direct simulation Monte Carlo and a hybrid-particle-in-cell method. Electrons were modeled as a massless fluid with a momentum equation that includes collisional contributions from ions and neutrals and an energy equation. Simulations of the laboratory PPT operating at discharge energies of 5, 20, and 40 J showed the expansion of the neutral and ion components of the plume during a pulse, the generation of low-energy ions and high-energy neutrals due to charge exchange reactions, and the generation of backflow. Numerical predictions showed good quantitative agreements with data.

Nomenclature

$\boldsymbol{E}$	=	electric field, Vm^{-1}
e	=	elementary charge, 1.6022×10^{-19} C
$\boldsymbol{F}_{ie}$	=	i–e collision force, N
I_{bit}	=	impulse bit, N-s
I_{sp}	=	specific impulse, s
$\boldsymbol{J}$	=	current density vector, Am^{-2}
k	=	Boltzmann constant, 1.3807×10^{-23} JK^{-1}
L	=	characteristic length
L_z, L_R	=	axial and radial size of the simulation domain, m
M_A	=	propellant mass ablated (injected) during a pulse, kg
$M_{I,N}$	=	total ion (neutral) mass ablated (injected) during a pulse, kg
$M_{i,n}$	=	ion i (neutral n) mass ablated (injected) during a pulse, kg
m_e	=	electron mass, 9.1094×10^{-31} kg
m_s	=	particle mass of species s, kg
$\dot{m}_s$	=	species s mass flow rate, kgs^{-1} m^{-2}
N_s	=	total number of computational macroparticles of species s
$\dot{N}_s$	=	number flux of species s particles,
$\langle N_e \rangle (r, \theta)$	=	time-average electron density
$n_e^{\max}(r, \theta)$	=	maximum electron density during a pulse, m^{-3}
$n_s(\boldsymbol{r}, t)$	=	number density of species s, m^{-3}
$n_{s,\max}$	=	maximum number density of species s, m^{-3}
n_0	=	background plasma density, m^{-3}
P	=	pulse duration, s
R, Z	=	radial and axial distances in the axisymmetric coordinate system, m
R_T	=	equivalent thruster radius, m
r, θ	=	polar coordinates measured from center of Teflon® bar, cm
S_s	=	speed ratio
s	=	species type, i for ions and n for neutrals
$T_{e\infty}$	=	background electron temperature, K
T_s	=	temperature of species s, K
$\langle T_e \rangle (r, \theta)$	=	time-average electron temperature
$U_{i,n}$	=	average drift velocity at the pulsed plasma thruster exit
u_s, v_s, w_s	=	axial, radial, and azimuthal drift components, ms^{-1}
$\boldsymbol{u}_s$	=	average (drift) particle velocity for species s particles
$\boldsymbol{v}_s$	=	particle velocity of species s
W_s	=	molecular weight of species s particle
X_s	=	species s mass fraction with respect to the total mass
$\boldsymbol{x}_s$	=	particle position vector
Z_i	=	number charge of ion i
ΔZ, ΔR	=	axial and radial cell width, m
ε_0	=	permittivity of free space, 8.854×10^{12} Fm^{-1}

Received 9 June 2000; revision received 18 December 2000; accepted for publication 2 February 2001.

*Associate Professor, Mechanical Engineering Department, 100 Institute Road. Senior Member AIAA.

†Space Grant Fellow and Graduate Research Assistant, Mechanical Engineering Department; currently Systems and Performance Engineer, GE Aircraft Engines, 1000 Western Avenue, Lynn, MA 01910. Student Member AIAA.

‡Graduate Research Assistant, Mechanical Engineering Department; currently Software Engineer, Nortel Networks, 600 Technology Park Drive, Billerica, MA 01821.

§Aerospace Engineer, On-Board Power and Propulsion. Member AIAA.

¶Aerospace Engineer, On-Board Power and Propulsion; currently Director, Systems and Technology Development, General Dynamics–Ordnance and Tactical Systems Aerospace Operations, P.O. Box 97009, Redmond, WA 98073-9709. Associate Fellow AIAA.

η = total propellant ionization fraction
λ_D = debye length, m
λ_{st} = mean-free path for collisions between s and t, m
ν_e = total electron collision frequency, s^{-1}
ν_{ie}^{ε} = average $i-e$ energy transfer collision frequency, s^{-1}
ν_{st} = average momentum transfer collision frequency for collisions between s and t, s^{-1}
ϕ = electric potential, V

Introduction

A PULSED plasma thruster (PPT) is a type of electromagnetic propulsion system that ablates, ionizes a solid Teflon® propellant, and then accelerates the plasma to generate thrust. The rectangular-geometry PPT shown schematically in Fig. 1 has been investigated since the 1960s, and interest has been renewed in the past half decade due to their specific impulses in excess of 1000 s, low-power requirements, simple propellant management, and the success of initial flight tests.[1–4]

Successful integration of PPTs on spacecraft requires the comprehensive evaluation of possible plume spacecraft interactions. The PPT plume consists of a series of plasma clouds (plasmoids) injected during the pulsed operation of the thruster. A plasmoid shown schematically in Fig. 1 consists of neutrals and ions from the partial decomposition of the Teflon propellant, particulates from erosion of electrodes and thruster components, and neutrals and ions produced by chemical reactions such as charge exchange, as well as electromagnetic fields and optical emissions. The majority of plume investigations was conducted in the early 1970s using the Lincoln (Laboratory) Experimental Satellite (LES-6) thruster[1,2,5–8] or specifically designed PPTs[8,9] with few studies appearing in the 1980s.[10] The renewed interest in PPTs prompted new plume investigations, using various derivatives of the flight-qualified LES-8/9.[4,11–19] Our current understanding of the PPT plumes indicates that they are more complex than those from other electric thrusters and fall in the category of unsteady, high-density, collisional, and partially ionized plasmas. In addition, the plasmadynamic processes in the PPT channel that determine the properties of the plume, are still under investigation.[4] These physical characteristics of the PPT plumes make experiments and modeling challenging. The goal of our research is to characterize the PPT plume and develop a predictive ability that will allow the assessment of potential plume/spacecraft interactions. Our PPT research combines experimental investigations[11,12,15,19] and modeling,[20–25] which are summarized in this paper.

Experimental Investigations

LES 8/9 PPT Plume Measurements[12]

The thruster used in these experiments was an LES 8/9 PPT. The experiments were carried out at NASA John H. Glenn Research Center Electric Propulsion Laboratory facilities using single langmuir probes, a fast ionization gauge, and a residual gas analyzer. At capacitor discharge energy of 20 J, this PPT ablates 28.5 μg of Teflon, and the pulse has a duration of 12 μs. The LES 8/9 has a canted exit channel, and these experiments used the nozzle extension described by Myers et al.[11] to make the nozzle symmetric. Initial studies using the LES 8/9 PPT included contamination assessment using quartz crystals, measurements of ion current density using planar langmuir probes, and determination of ion velocity using single langmuir probes.[11] It was found that measurable changes in transmittance of the quartz samples were confined to 30 deg, the centerline ion velocity was approximately 40 km/s, and the ion density 6×10^{18} m^{-3} at a distance of 24 cm from the thruster.[11]

The LES 8/9 PPT was mounted on a support arm at the top of a 3-m-high, 1.5-m-diam vacuum tank shown in Fig. 2. The tank was cryopumped to a base pressure of approximately 10^{-7} torr with a time-averaged pressure during several hours of thruster firings of approximately 6×10^{-6} torr. A movable, computer-controlled probe rake was built that allowed many readings to be taken without repressurizing the vacuum facility and manually repositioning the probes. The rake was designed so that the fast ionization gauge, the single langmuir probe, and the nozzle of the thruster were aligned, allowing time of flight measurements to be taken. A schematic of the probe rake mounted in the tank is shown in Fig. 3.

Single langmuir probe data were collected at 0, 20, 40, 60, and 90 deg from the centerline of the PPT nozzle, in the plane perpendicular to the thruster electrode surfaces. Five pulses were recorded at each position, and at all measurement locations, each probe trace showed an initial large current peak followed by a smaller peak. This pattern seems to indicate the presence of two ion groups associated

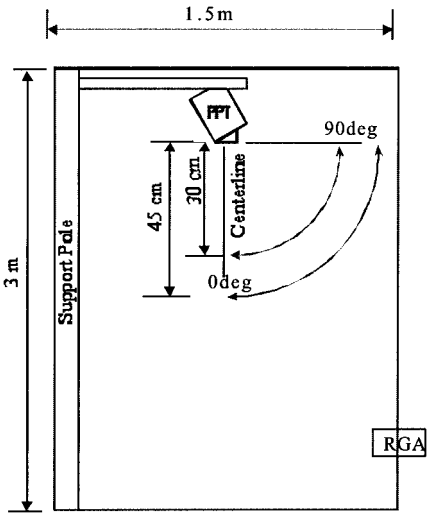

Fig. 2 Experimental apparatus used in the LES 8/9 PPT plume investigation.

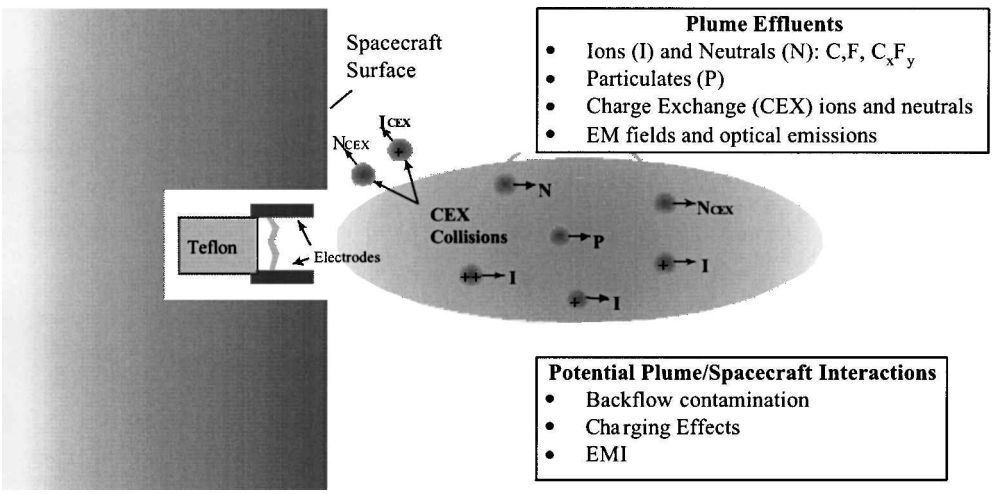

Fig. 1 Rectangular PPT schematic and its plume effluents.

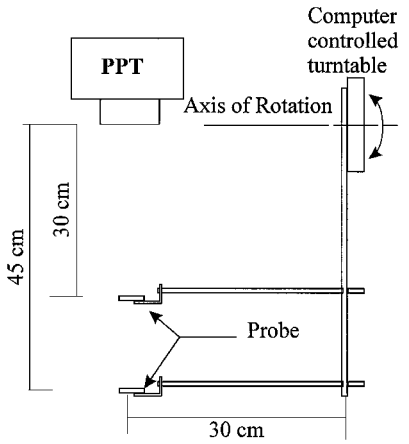

Fig. 3 Schematic of the probe motion system used in the LES 8/9 PPT plume investigation.

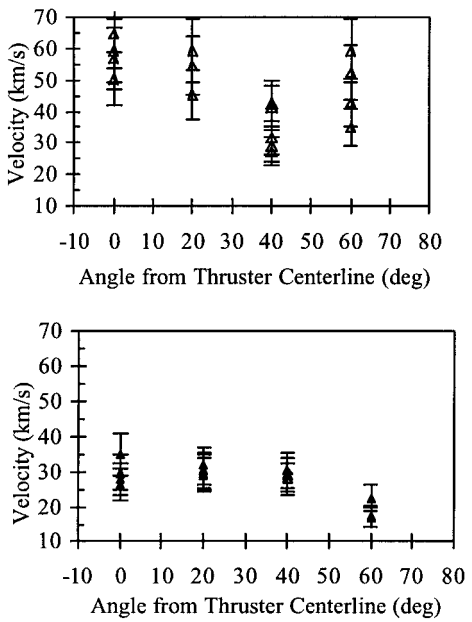

Fig. 4 Speed of ions based on time-of-flight langmuir probe measurements in the plume of the LES 8/9 PPT.

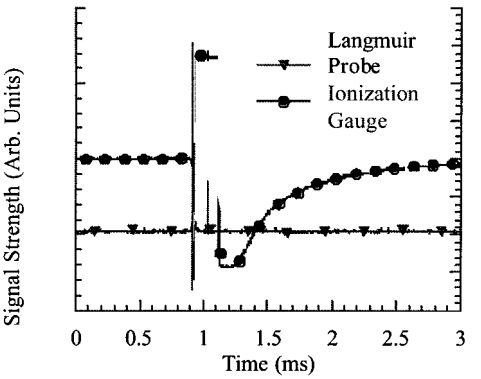

Fig. 5 Fast ionization gauge and single langmuir probe traces in the plume of the LES 8/9 PPT; radial distance is 0.3 m, and the angle is 40 deg.

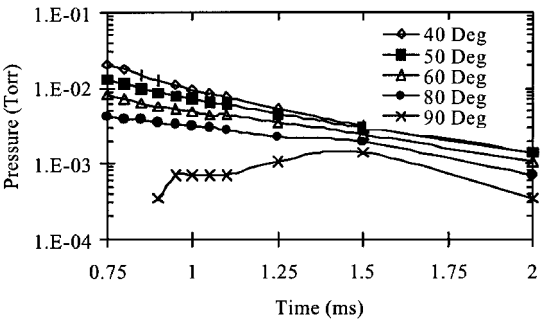

Fig. 6 Pressure evolution from fast ionizaton gauge measurements in the plume of the LES 8/9 PPT.

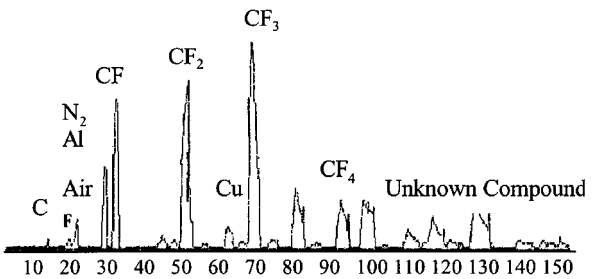

Fig. 7 Residual gas analyzer trace of vacuum tank after firing of the LES 8/9 PPT.

with each current peak in the plume. Speed estimates were obtained using $V = D/T_f$, where $D = 0.15$ m is the distance between the probes and T_f is the time for each current peak to travel between the two aligned probes. Ion speed estimates are shown in Fig. 4 with error estimated at $\pm 16.6\%$.

Our analysis shows that the first current peak is associated with ions moving in excess of 60 km/s at the centerline. The second current peak provides ion speeds that agree with those found previously for the LES 8/9 thruster,[11] with an average centerline velocity of approximately 30 km/s. Analysis of the second current peak shows a significant decrease in ion speed at 40 deg that has been noted in earlier studies. There are several possible explanations for the multiple groups of ions that have been observed. Thomassen and Vondra[6] found that faster moving multiply ionized particles are produced during the early stages of the PPT pulse. Therefore, the first current peak could be associated with these faster particles, and the subsequent peak associated with slower, singly charged particles. Another possible cause of the multiple current peaks in the plume could be the current reversal observed during the PPT capacitor discharge. Using the derived centerline speeds and back-tracing of the fast and slow ions showed that the fast group was created on average 3 μs before the slow group. This value is very close to the period of current reversal seen in current discharge data from the LES 8/9.

Figure 5 shows a sample of fast ionization gauge and single langmuir probe traces during the PPT pulse, taken at 0.3 m downstream and 40 deg off the centerline. The saturation of the fast ionization gauge due to the plume ions is clearly shown for up to approximately 750 μs after the beginning of the pulse. Figure 6 shows late-time pressure in the plume derived from the ionization gauge data for various angles taken at an axial distance of 0.3 m downstream of the nozzle exit. These pressure measurements are taken long after the ionized portion of the plasmoid passed (approximately 730 μs), indicating the presence of slow neutral particles in the PPT plume. It is very difficult to quantify the uncertainty in fast ionization gauge measurements, because many interdependent factors, such as gauge sensitivity, relative sensitivity, and plume composition, come into play. Estimates of neutral particle speed can also be obtained from ionization gauge data. Assuming that all neutral particles are released at the start of the pulse, the neutral particle speed is found to be between 100 and 1000 m/s.

A residual gas analyzer output of the LES 8/9 PPT plume is shown in Fig. 7. There are three obvious main peaks on the analyzer trace, at 31, 50, and 69 atomic mass unit (amu) corresponding to CF, CF_2, and CF_3, respectively. A peak at 12 amu indicates carbon. The smaller peaks at 16 and 18 are due mainly to air; however fluorine has an atomic mass of 19 and is potentially being detected here as well. If aluminum from the thruster body and exhaust channel were present in the trace with a peak at 27, it would be hard to distinguish from the N_2 at 28 amu. The small peak at 44 is due to background CO_2. It

is also likely that the peak near 63 amu is due to copper eroded from the thruster's electrodes, whereas the peak near 88 amu can be attributed to CF_4. The peaks above about 70 amu could be molecules eroded from the composite nozzle extension or from impurities in the Teflon. It is unlikely that they result from pump oils because they did not appear in traces taken in the tank when the thruster was off. The residual gas analyzer trace shows that the plume consists of molecules consistent with previous studies.[10] No conclusion should be drawn from the relative heights between these three constituents. Because the analyzer was placed on the differential pump during calibration, it was impossible to determine the pressure of the gas being sampled and, thus, to calibrate the analyzer's sensitivity. The accuracy of the analyzer used in this investigation is tenuous at best. The sampling time of the analyzer used in this study is on the order of 1 min, much longer than the pulse period and, thus, provides enough time for equilibrium of the gas in the tank facility and possible reactions between the plume species to occur. What is being detected, then, is the equilibrium products of the plume and not the composition of the plasmoid as it leaves the thruster.

Laboratory PPT Plume Measurements[19]

In this investigation, triple langmuir probes were used to measure simultaneously electron temperatures and electron densities in the plume of a laboratory PPT. The thruster shown in Fig. 8 has a rectangular geometry with 2.5-cm square electrodes and was designed for component life tests and plume characterization. The thruster is almost identical in size and performance to the LES 8/9 model, and the operational characteristics are shown in Table 1.

Previous PPT plume investigations of plasma density and temperature have used interferometers, and single and double langmuir probes.[7,8,26] Triple Langmuir probes offer many advantages over these methods, allowing simultaneous measurement of T_e and n_e

Table 1 Parameters used as inputs in the laboratory PPT plume simulations

	E_D, J		
Parameter	S	20	40
	Known		
A, cm^2	17.1	17.1	17.1
P, μs	10	15	15
I_{bit}, μN-s	36	256	684
M_a, μg	10.6	26.6	51.3
	Assumed		
s	C, F, C^+, F^+	C, F, C^+, F^+	C, F, C^+, F^+
M_I, μg	1.06	7.98	15.4
u_I, km/s	8	20	34
$T_i(r, z_E)$, eV	1	1	1
$T_n(r, z_E)$, eV	1	1	1
	Derived		
M_N, μg	9.54	18.6	35.9
u_N, km/s	2.89	5.18	4.48
$n_{C^+\max}$, m^{-3}	3.19×10^{20}	8.56×10^{20}	9.71×10^{20}
$n_{F^+\max}$, m^{-3}	2.02×10^{20}	2.7×10^{20}	3.06×10^{20}
$n_{C\max}$, m^{-3}	3.12×10^{21}	6.57×10^{20}	1.45×10^{21}
$n_{F,\max}$, m^{-3}	7.67×10^{21}	6.88×10^{21}	1.53×10^{22}

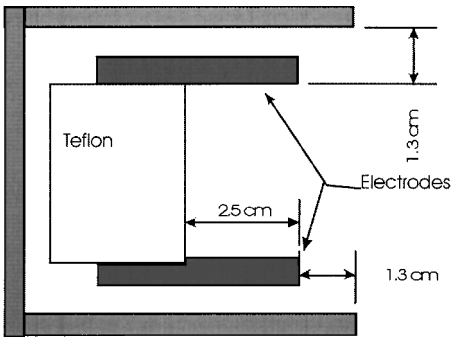

Fig. 8 Schematic of laboratory PPT used in triple langmuir probe plume investigation.

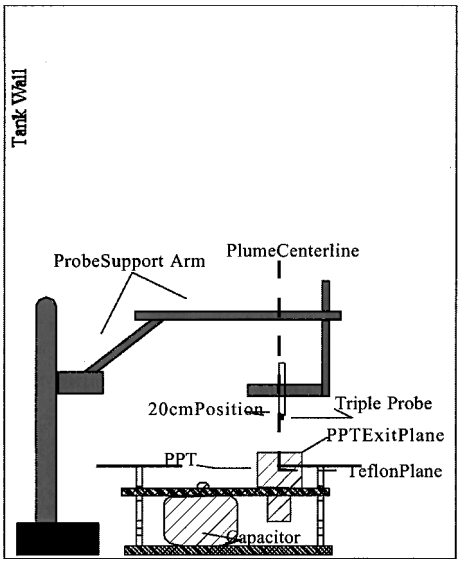

Fig. 9 Experimental apparatus used in the triple langmuir probe investigation of the laboratory PPT plume.

(Refs. 27–29). Unlike single and double langmuir probes, the triple langmuir probe does not require voltage sweeps, a task that is difficult in the PPT due to both its pulsed nature and the pulse-to-pulse variation. Additionally, triple probes are relatively easy to set up and operate and do not require the extensive optics of an interferometer. A symmetric triple langmuir probe, similar to the ones used in our experiments, consists of three identical probes placed in the plasma. One of the probes, indicated as probe-2, for example, is allowed to float in the plasma and a fixed voltage V_{d3} is applied between the positive and negative with respect to the floating potential probes. The resulting voltage difference $V_{d2}(t)$ and collected current $I(t)$ allow the evaluation of $T_e(t)$ and $n_e(t)$. Triple probes have been used successfully in the steady plumes of arcjets,[30] the magnetoplasma dynamic thruster,[30,31] and gasdynamic PPTs.[32]

Experiments were conducted in a 0.5-m diam, 1-m-tall bell jar under base pressures between 1×10^{-5} and 5×10^{-5} torr. The thruster was placed at the bottom of the facility, firing upward, with the probes mounted on a vertical translation table that was computer controlled outside of the tank. This arrangement is shown in Fig. 9. For off-centerline measurements, the thruster was rotated through the appropriate angle, with the probe aligned geometrically with the center of the Teflon face.

For each discharge energy level of 5, 20, and 40 J, measurements were taken at eight downstream locations, ranging from 6 to 20 cm from the Teflon surface in 2-cm increments. These measurements were taken at polar angles of 10, 20, and 30 deg on two planes perpendicular and parallel to the electrodes passing through the thruster's centerline. Additionally, measurements were taken at 45 deg off centerline on the plane perpendicular to the thruster electrodes. These locations are shown in Fig. 10. Five pulses were recorded at each location and at each power level, resulting in nearly 1000 data sets.

Implementation of the triple probe in the PPT plume requires careful consideration of plasma and probe parameters that enter in the evaluation of $T_e(t)$ and $n_e(t)$. These issues are discussed extensively in Ref. 19, but we review some important aspects.

The uncertainty in the triple-probe measurements comes from the processing of the voltage $V_{d2}(t)$ and current signals $I(t)$, as well the triple-probe theory itself. The voltage probes and oscilloscope used to record $V_{d2}(t)$ introduced a high-frequency bit error in the temperature measurements with a maximum of ± 0.75 eV occurring at the peak of the pulse. The noise in the current measurements was minimal, and the effect of the voltage noise introduced a $\pm 10\%$ uncertainty into the density measurements. The uncertainty in temperature measurements for the regime of probe operation was estimated to be smaller than 20% and in electron density between 40 and 60%. Therefore, for all measurements, the maximum uncertainty

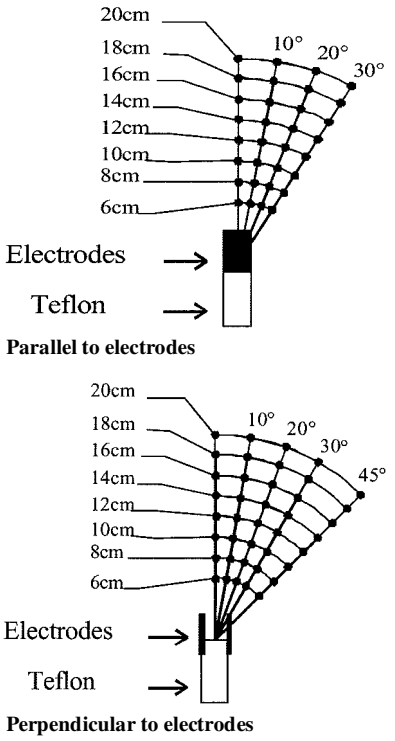

Fig. 10 Triple langmuir probe measurement locations on the parallel and perpendicular to the electrode plane passing through thruster centerline; radial and angular positions are referenced with respect to center of Teflon surface.

in $n_e(r, \theta, t)$ is estimated to be 60%, the maximum uncertainty in $T_e(r, \theta, t)$ is ± 0.75 eV, and the spatial accuracy is within $\pm 10^{-2}$ m.

An important issue in proper interpretation of triple probes in flowing plasmas is that of probe/flow alignment. In our experiments, the triple probe was aligned with the polar angle measured from the center of the Teflon surface, and this may have resulted in probe misalignment with the flow vector. Investigations using a PPT similar to the one used in our experiment showed that the plume is canted toward the cathode by less than 5 deg on the plane perpendicular to the electrodes and confirmed that the plume is symmetric on the parallel to the electrodes plane.[17,18] An assessment of the impact on the triple-probe output due to the flow/probe misalignment showed that the effects did not adversely affect our measurements.[19] In addition, the end-effects parameter was conservatively estimated to be $\tau_L \gg 230$, further ensuring that the ion current is not sensitive to any small misalignments between the probe and the flow vector.[19]

Figure 11 shows typical electron density and electron temperature traces for the 20-J case for $r = 6$ and $r = 18$ cm at $\theta_\perp = 10$ deg on the perpendicular plane. The bounding traces are plotted for each location, showing the shot-to-shot variability, as well as the unsteady character of the plasmoids as they pass by the triple probe.

Simultaneous electron temperature and density for a 20-J pulse measured $r = 12$ cm and $\theta_\perp = 10$ deg are plotted in Fig. 12. In most cases, the maximum electron temperature for each spatial location occurs at the beginning of the pulse, when the most energetic electrons leave the thruster, whereas the maximum electron density occurs near the middle of the pulse.

The time-average electron temperature $\langle T_e \rangle$ for a location (r, θ) over the duration of the pulse is obtained by

$$\langle T_e \rangle(r, \theta) = \sum_N \left[\int_0^P T_e(r, \theta, t)\, \mathrm{d}t \Big/ P \right] \Big/ N \qquad (1)$$

where $N = 5$. A similar expression gives the time-average electron density $\langle N_e \rangle(r, \theta)$.

Figures 13–15 show the time-average plume properties for a 5-, 20-, and 40-J discharge, respectively. The time-average density drops by almost an order of magnitude within and radial distance

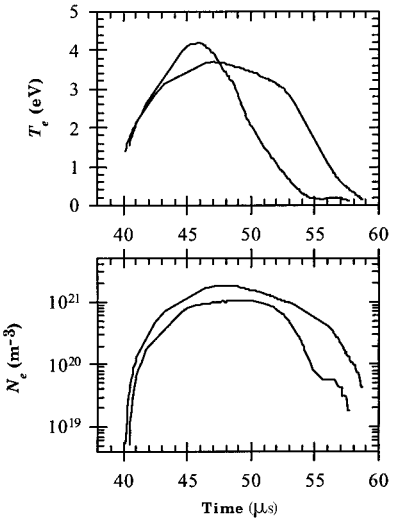

a) $r = 6$ cm, $\theta_\perp = 10$ deg

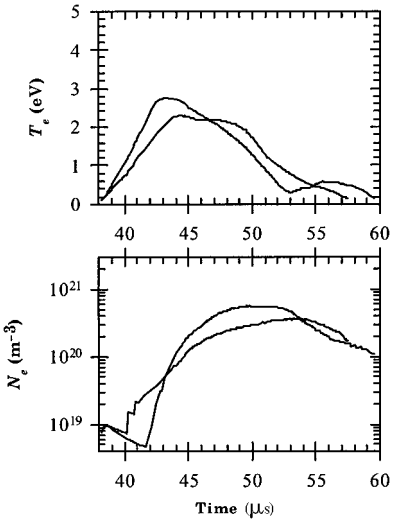

b) $r = 18$ cm, $\theta_\perp = 10$ deg

Fig. 11 Electron temperature and density traces obtained from triple langmuir probe in the plume of a 20-J laboratory PPT.

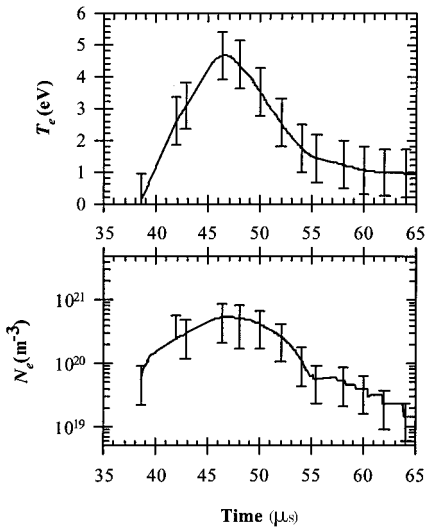

Fig. 12 Electron temperature and density in the plume of a 20-J laboratory PPT measured at $r = 12$ cm and $\theta_\perp = 10$ deg.

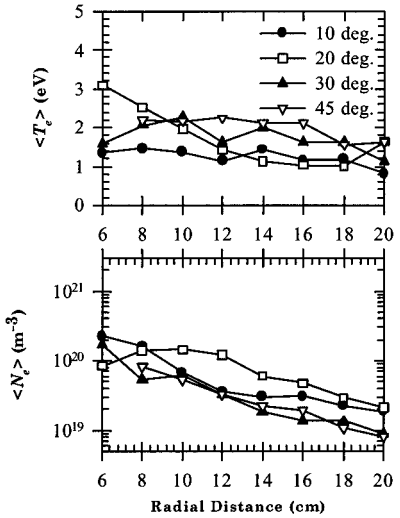

a) Perpendicular plane

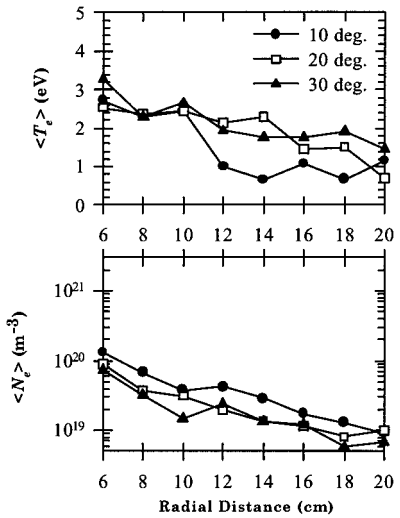

b) Parallel plane

Fig. 13 Spatial variation of time-averaged electron density $\langle N_e \rangle$ (± 60%) and temperature $\langle T_e \rangle$ (± 0.75 eV) in plume of 5-J laboratory PPT.

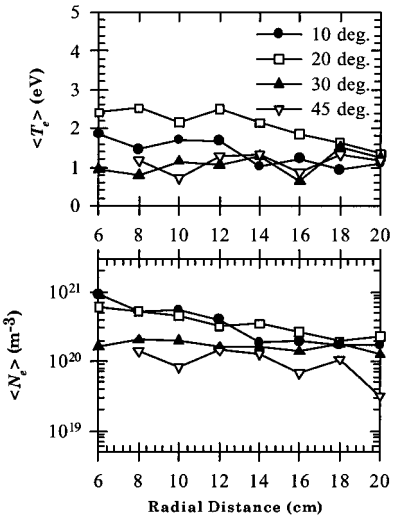

a) Perpendicular plane

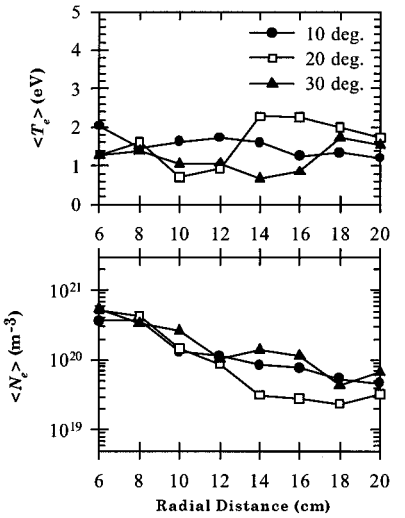

b) Parallel plane

Fig. 14 Spatial variation of time-averaged $\langle N_e \rangle$ (± 60%) and $\langle T_e \rangle$ (± 0.75 eV) in the plume of a 20-J laboratory PPT.

of 12 cm downstream from the PPT exit. The measurements show particularly well the large angular variation of density in the perpendicular plane and the high degree of uniformity in the parallel plane. For all cases considered, time-average electron temperature is ~3 eV at 6 cm and decreases to ~1 eV at 20 cm from the Teflon surface. These magnitudes compare with recent spectroscopic measurements in a PPT plume.[13] From these data, it can be concluded that increasing the discharge energy results in larger time-average electron densities for all plume locations. The time-average electron temperature, however, remains unaffected within the accuracy of our measurements. These effects should be reexamined with higher-fidelity measurements.

PPT Plume Modeling[24,25]

Computational modeling complements our PPT plume experimental investigations. We present next a summary of the hybrid (particle–fluid) PPT plume model, simulation results, and comparisons with data.

Hybrid (Particle–Fluid) Model Description

The plume model includes neutrals, for example, C and F, and ions, for example, C^+ and F^+, from the Teflon decomposition. A hybrid representation is chosen to model the physical characteristics of the PPT plume components. The unsteady character of the plume is considered as a series of plasmoids ejected from the exit of the thruster channel during the thruster firing. The code incorporates a single grid and subcycling for the time integration. The axisymmetric simulation domain in Fig. 16 is discretized using a structured nonuniform grid. Cells scale with the local mean-free path and are further divided also in subcells and used for evaluation of collisions. The vertices of each cell are the nodes where the average (fluid) quantities are evaluated.

Neutrals and ions are treated as particles using concepts of the direct simulation Monte Carlo (DSMC)[33] and a hybrid-particle-in-cell (hybrid-PIC) approach that includes a collisional ion–electron force.[34] The kinetic description of ions and neutrals is necessary and allows evaluation of fluxal properties needed for future contamination characterization. The distribution function of a plume species s with mass m_s, number density $n_s(\boldsymbol{r}, t)$, average (or drift) species velocity $\boldsymbol{u}_s(\boldsymbol{r}, t) = \langle \boldsymbol{v}_s \rangle \equiv (u_s, v_s, w_s)$, and temperature T_s is given by a local Maxwellian. Each species s macroparticle (or simulation particle) represents F_s number of real plume particles. A total of N_s macroparticles reside in the simulation domain with the kth macroparticle described by a set of position and velocity $\{\boldsymbol{x}_{sk}, \boldsymbol{v}_{sk}\}$, $k = 1, N_s$. Neutral and ion particles move and undergo collisions that include neutral–neutral elastic, ion–neutral elastic, ion–neutral charge exchange and ion–electron.

The modeling of elastic neutral–neutral and neutral–ion particle collisions and motion is accomplished by the non-time-counter (NTC) method described by Bird.[33] Ions and neutrals in the model include those created by the charge exchange (CEX) reaction

$$X^n_{\text{slow(fast)}} + X^+_{\text{(fast)slow}} \longrightarrow X^n_{\text{(fast)slow}} + X^+_{\text{slow(fast)}} \qquad (2)$$

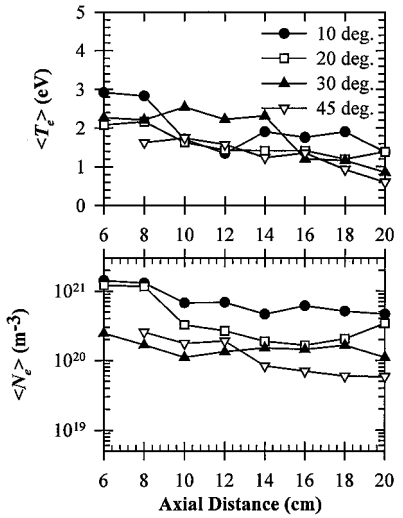

a) Perpendicular plane

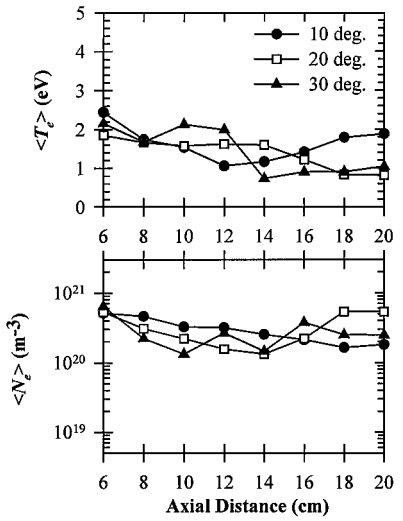

b) Parallel plane

Fig. 15 Spatial variation of time-averaged $\langle N_e \rangle$ (± 60%) and $\langle T_e \rangle$ (± 0.75 eV) in the plume of a 40-J laboratory PPT.

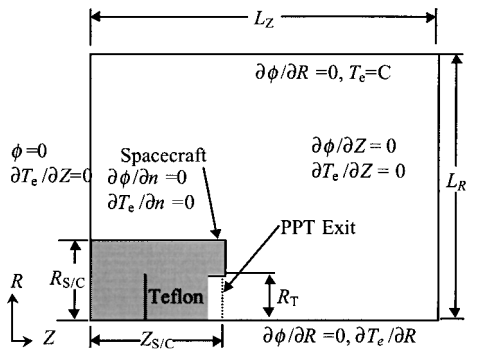

Fig. 16 Computational domain used in the laboratory PPT plume simulations.

The low-energy CEX species are of particular importance to backflow and possible spacecraft contamination.[35] The NTC methodology is used to determine the number of possible CEX partners in each cell with appropriate CEX cross sections, whereas the postcollision velocities of the reacting particles are simply exchanged.

After the collision process has been completed in all cells, a particle with a postcollision velocity $\boldsymbol{v}_s$ is moved according to

$$\frac{\mathrm{d}\boldsymbol{x}_s}{\mathrm{d}t} = \boldsymbol{v}_s \tag{3}$$

For an ion particle with position $\boldsymbol{x}_i$, and charge q_i the equation of motion includes the electric field force $q_i\boldsymbol{E}$ as well as a collision force $\boldsymbol{F}_{ie}$:

$$m_i \frac{\mathrm{d}\boldsymbol{v}_i}{\mathrm{d}t} = q_i\boldsymbol{E}(\boldsymbol{x}_i) + \boldsymbol{F}_{ie}(\boldsymbol{x}_i) \tag{4}$$

The electric field and the collision force in Eq. (4) needed at the ion position $\boldsymbol{x}_i$ are evaluated from the cell-vertex (nodal) values. The collision force at the nodes incorporates ion–electron collisions into the PIC method and is given by Jones et al.[34] as

$$\boldsymbol{F}_{ie} = \nu_{ie} m_{ie}(\langle \boldsymbol{v}_e \rangle - \langle \boldsymbol{v}_i \rangle) + (\langle \boldsymbol{v}_i \rangle - \boldsymbol{v}_i) \times \left(\frac{\nu_{ie}^{\varepsilon} k(T_i - T_e)}{\langle \boldsymbol{v}_i^2 \rangle - \langle \boldsymbol{v}_i \rangle^2} - \frac{\nu_{ie} m_{ie}^2 (\langle \boldsymbol{v}_e \rangle - \langle \boldsymbol{v}_i \rangle)^2}{m_i \left(\langle \boldsymbol{v}_i^2 \rangle - \langle \boldsymbol{v}_i \rangle^2 \right)} \right) \tag{5}$$

where $m_{ie} = m_i m_e/(m_i + m_e)$ is the reduced mass, ν_{ie} is the dynamic friction collision frequency, ν_{ie}^{ε} the energy transfer collision frequency, and brackets indicate averaging over the species distribution function. The average (or fluid) ion quantities in Eq. (5), $\langle \boldsymbol{v}_i \rangle = \boldsymbol{u}_i$, $\langle \boldsymbol{v}_i^2 \rangle$, and $\langle \boldsymbol{v}_i \rangle^2$, and T_i are obtained at a grid point from interpolation of all particles in the surrounding cells.

Unlike other DSMC/PIC plume studies[35–39] and our previous plume work[20,21] that utilized the Boltzmann approximation for the electrons, in this work electrons are modeled as a massless fluid with a momentum equation that includes collisional contributions from ions and neutrals. The average velocity of electrons at a grid point $\langle \boldsymbol{v}_e \rangle = \boldsymbol{u}_e$ is obtained from a fluid model. Based on scaling analysis[25] unsteady, inertia, and magnetic terms are ignored, and the electron momentum equation becomes

$$\boldsymbol{u}_e = -\frac{e\boldsymbol{E}}{m_e \nu_e} - \frac{1}{n_e m_e \nu_e} \nabla p_e + \left(\sum_i \nu_{ei} \boldsymbol{u}_i \Big/ \nu_e \right) + \left(\sum_n \nu_{en} \boldsymbol{u}_n \Big/ \nu_e \right) \tag{6}$$

where ν_e is the total electron collision frequency. The mean (fluid) ion $\boldsymbol{u}_i$ and neutral $\boldsymbol{u}_n$ velocities are obtained from interpolation of particle velocities in the surrounding cells. In the PPT plume even at electron densities $n_e \leq 10^{17}$ m^{-3}, where $\nu_{ei} \leq 10^5 \mathrm{s}^{-1}$, electron–neutral collisional terms in the momentum equation may become of the same order as the pressure gradient or the electric term. Therefore, the full form of the reduced electron momentum equation (6) is used in this model.

Based on scaling analysis[23] the electron temperature is modeled with a form of the energy equation that includes the conductive and collisional transfer terms as

$$0 = -\nabla \cdot K_e \nabla T_e - \sum_{H=i} 3 \frac{m_e}{m_H} \nu_e n_e k (T_e - T_H) \tag{7}$$

where K_e is the electron conductivity. The boundary conditions on the upper far-field boundary are[23,35]

$$T_e = \sqrt[p+1]{(R_T/r)\left(T_{e0}^{p+1} - T_{e\infty}^{p+1}\right) + T_{e\infty}^{p+1}} \tag{8}$$

where T_{e0} is the temperature at the thruster exit, $T_{e\infty}$ is the background temperature, and p is a temperature-dependent index.[23] Boundary conditions on the other sides of the domain are shown in Fig. 16.

Electric fields are obtained from a formulation of the current conservation equation that allows discretization at scales larger than the debye lengths λ_D, which for plasma densities of $n_e \approx 10^{17}$–10^{21} m^{-3} and $T_e \approx 1$–5 eV is in the range of 10^{-5}–10^{-7} m. Assuming quasi neutrality, the electron density is given by

$$n_e \cong \sum_i n_i \tag{9}$$

Current conservation under quasi neutrality can be written as

$$\nabla \cdot \boldsymbol{J} = 0 \tag{10}$$

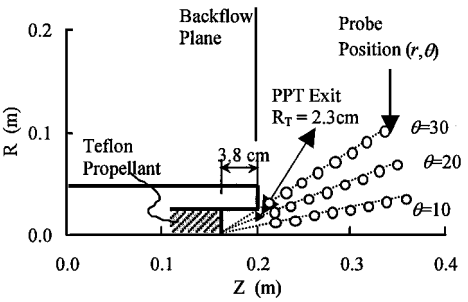

Fig. 17 Virtual triple-probe locations used in the laboratory PPT plume simulations.

where the total current density is

$$\boldsymbol{J} = \sum_s n_s q_s \boldsymbol{u}_s = \sum_i q_i n_i \boldsymbol{u}_i - e n_e \boldsymbol{u}_e \tag{11}$$

or

$$\nabla \cdot \left(\frac{e^2 n_e}{m_e \nu_e} \boldsymbol{E} \right) = -\nabla \cdot \left(\sum_i n_i q_i \boldsymbol{u}_i \right) - \nabla \cdot \left(\frac{e}{m_e \nu_e} \nabla p_e \right) - \nabla \cdot \left(-e n_e \sum_i \nu_{ei} \boldsymbol{u}_i \Big/ \nu_e \right) - \nabla \cdot \left(-e n_e \sum_n \nu_{en} \boldsymbol{u}_n \Big/ \nu_e \right) \tag{12}$$

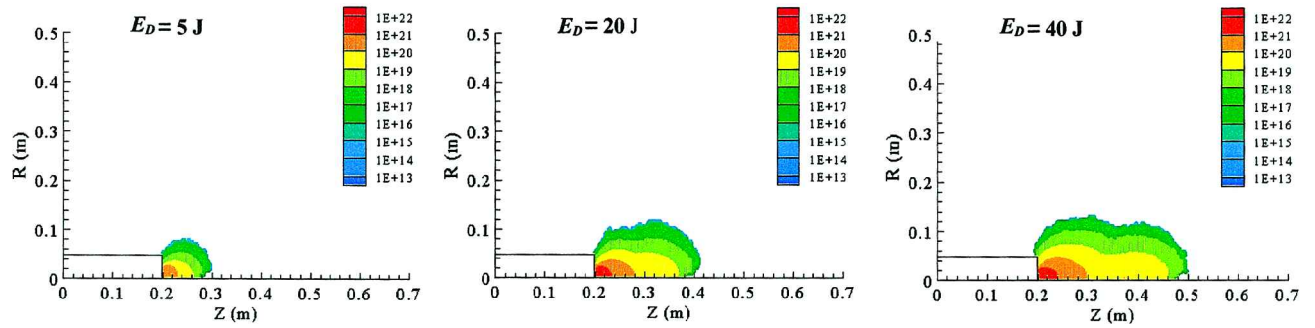

a) Ion number density (m^{-3}) at $t = 0.5\,P$

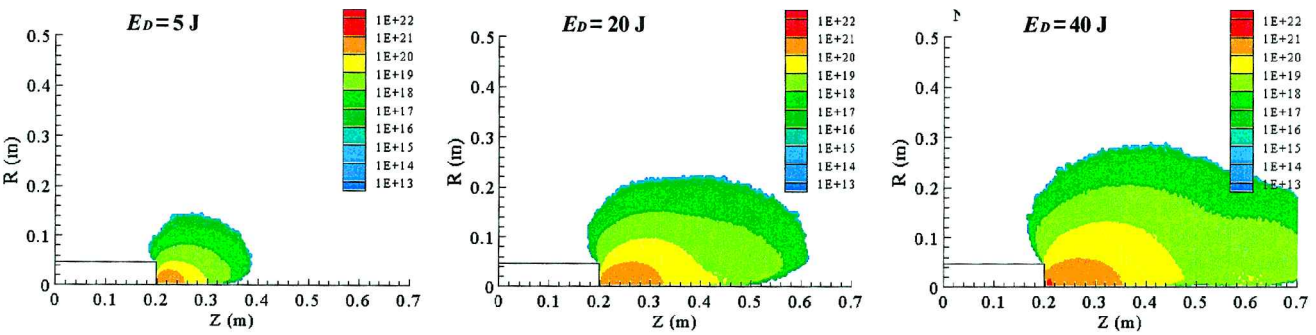

b) Ion number density (m^{-3}) at $t = P$

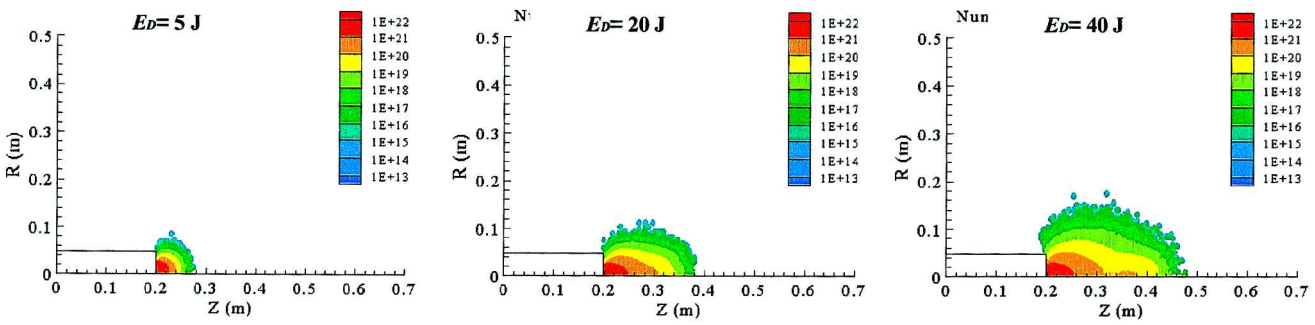

c) Neutral number density (m^{-3}) at $t = 0.5\,P$

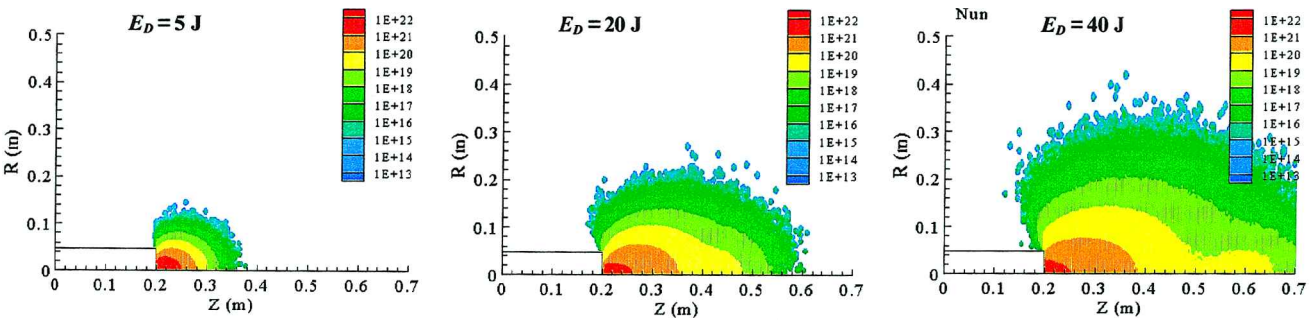

d) Neutral number density (m^{-3}) at $t = P$

Fig. 18 Ion and neutral number density from the simulation of the laboratory PPT plume at discharge energy of 5, 20, and 40 J.

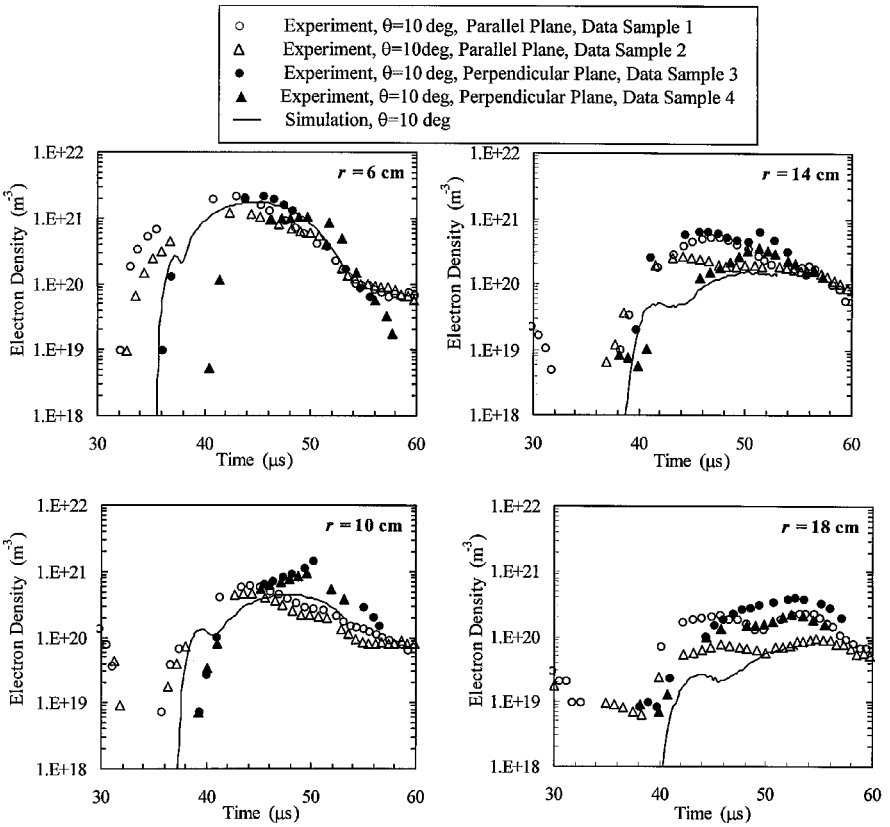

Fig. 19 Comparisons between electron number density predictions and experimental data in the plume of a 5-J laboratory PPT; time shown is that of experiment.

The charge $n_e = n_i$ on the nodes is obtained through weighting of the charge of the particles found in the cells surrounding the node using a conservative weighting scheme. Electric fields are electrostatic given by a potential ϕ as $\boldsymbol{E} = -\nabla\phi$. The electric field and temperature are obtained on the grid points from central finite differencing of Eqs. (7) and (12) with appropriate boundary conditions. Solution of the resulting matrix equations is based on a version of the restarted generalized minimum residual solver with incomplete lower–upper factorization.[23]

Modeling Results

A series of simulations was performed using the laboratory PPT shown schematically in Figs. 16 and 17. Particle injection at the PPT exit is based on a model that assumes complete decomposition of the Teflon and accounts for the ablated mass and impulse during the pulse:

$$M_A = \sum_i M_i + \sum_n M_n = M_I + M_N = aW_{C_2F_4} \qquad (13)$$

$$I_{\text{bit}} = \sum_i M_i u_i + \sum_n M_n u_n = M_I U_i + M_N U_n \qquad (14)$$

The density is given by a profile

$$n_s(R, Z_E, t) = n_{s,\max} \sin[\pi(t - t_1)/P]\left[1 - (1 - C_c)(R/R_T)^2\right]$$
$$t_1 \le t \le t_2 \qquad (15)$$

where $P = t_1 - t_2$ is the duration of the pulse, R_T is the equivalent radius of thruster exit, and C_c is the cutoff density ratio. The assumed sinusoidal time-variation $n_s(t)$ follows the evolution of the PPT discharge current, as well as the electron density variation measured at the near-exit region of the PPT. The radial variation is based on PPT-channel simulations that indicate that density profiles are parabolic.[40] The maximum density $n_{s,\max}$ is given by

$$n_{s,\max} = 4M_s \Big/ W_s \bar{c}_s \left\{\exp\left(-S_s^2\right) + \sqrt{\pi} S_s [1 + \text{erf}(S_s)]\right\} P(1 + C_c) R_T^2 \qquad (16)$$

A sinusoidal electron temperature profile is used at the exit plane given by

$$T_{e0} = (T_{e,\max} - T_{e\infty}) \sin[\pi(t - t_1)/P] + T_{e\infty} \qquad (17)$$

where $T_{e,\max}$ is the experimentally determined maximum electron temperature.

An axisymmetric nonuniform grid was used in the simulations. The last-to-first cell ratios A_Z and A_R are set to values so that widths of the cells in the downstream region of the PPT exit scale with the smallest mean-free paths expected during the plasmoid propagation. In the simulations $L_Z = L_R = 1$m, $N_Z = 320$, $N_R = 150$, $A_Z = 1.0795$, and $A_R = 2.7859$ resulting to $\Delta Z_{\min} = 3.007$ mm, $\Delta R_{\min} = 3.822$ mm, $\Delta Z_{\max} = 3.246$ mm, and $\Delta R_{\max} = 10.648$ mm. The cells are also divided into four subcells in both directions and used for sampling of collision partners. The cell and subcell widths used in the simulations scale even with the most restrictive mean-free paths. The total number of computational particles at the end of the pulse is 480,590 ions and 3,920,001 neutrals for the 5-J case, 1,271,338 ions and 2,525,192 neutrals for the 20-J case, and 1,258,637 ions and 1,339,862 neutrals for the 40-J case. Time steps are $\Delta t_i = 0.05$ μs and $\Delta t_n = 0.1$ ms for all cases considered. The input parameters necessary for particle injection obtained using the thruster exit model are shown in Table 1. The assumed parameters are chosen carefully and are consistent with current knowledge of PPTs internal and plume flows. The plume composition is based on complete ablation of Teflon but inclusion of additional species would not affect the overall evolution of the plume. The ionization fraction and ion speed are taken so that the derived exit-model ion number densities are close to the measured ones in the plume. The neutral temperature is based partially on the assumption that neutrals do not exceed their sonic speed at the PPT exit. Finally, the ion temperature is set to equal that of the neutrals, although as a parameter temperature plays a secondary role due to the supersonic speed of the ions.

Figure 18 shows the time evolution of the ion and neutral components of the plasmoid for the 5-, 20-, and 40-J cases. At $t = 0.5P$

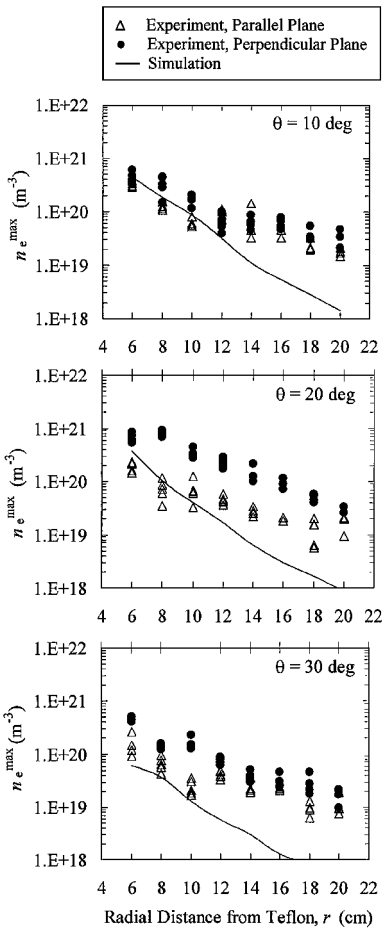

Fig. 20 Comparison between predicted and measured maximum electron number density in the plume of a 5-J laboratory PPT.

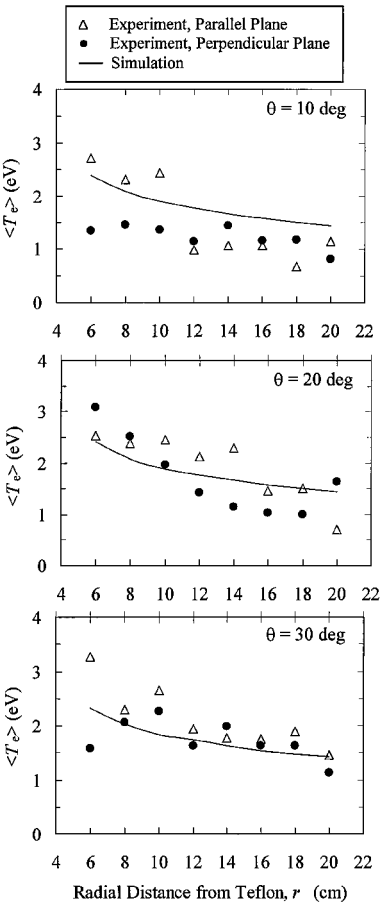

Fig. 21 Comparison between predicted and measured time-averaged electron temperature in the plume of a 5-J laboratory PPT.

the ion cloud is farther downstream than the neutral cloud due to the large average speeds of the ions. However, CEX reactions in the plume generate fast neutrals and slow ions, and as a result at $t = P$, both ion and neutral clouds have similar spatial extents. Figure 18 shows also the radial expansion of the ion cloud primarily due to radial electric fields and the radial expansion of the neutral cloud primarily due to pressure diffusion. The discharge energy and, therefore, ablated Teflon mass affect considerably the spatial extent of the plasmoid. As Fig. 18 shows, the spatial extent of the plasmoid and the backflow component increases with increasing ablated mass.

Comparisons with Experiments

Figure 17 shows the location of the virtual probes used in the simulations. To compare with the experiment shown in Fig. 10, a polar coordinate system (r, θ) is used where distances and polar angles are referred with respect to the center of the Teflon propellant, which is located 3.8 cm behind the PPT exit. We summarize comparisons between electron density and temperature predictions and our triple langmuir probe plume data.

Figure 19 shows the time evolution of the electron number density along the $\theta = 10$ deg line and distances from the Teflon propellant between 6 and 18 cm for the $E_D = 20$ J case. In Fig. 19 two data sets are plotted for each plane to indicate the pulse-to-pulse variation of density during the experiments, as well as the density differences between the planes parallel and perpendicular to the PPT electrodes. The time shown in Fig. 19 is that of the experiment, and to facilitate the comparisons, the simulation $t = 0\ \mu$s corresponds to $t_{\text{exp}} = 35\ \mu$s. Figure 19 shows clearly that the simulation results follow the data closely for all radial distances considered.

Figure 20 shows comparisons between the predicted and experimental maximum electron density for the 5-J laboratory PPT. The numerical predictions are of the same order as measurements for distances of up to $r = 12$ cm. The underprediction increases with distance from the Teflon, and for $r = 20$ cm the numerical values is an order of magnitude smaller than the measurements. A comparison between predicted and experimental time-average electron temperature for the 5-J PPT is shown in Fig. 21. The numerical predictions follow the data for the entire range of radial distances and angles.

There are several possible explanations for these differences between numerical predictions and the experiment. The relatively small 0.5×1 m cylindrical chamber used in our experiments may have inhibited the expansion of the plasmoid, resulting in higher densities compared with the simulations. There is also experimental uncertainty, which for the electron density has been estimated at 60% and for the electron density at ± 0.75 eV assuming perfectly aligned probes.[19] Finally, model assumptions as well as input conditions may have attributed to the differences between predictions and measurements. These comparisons also show that the axisymmetric simulations fail to capture the three dimensionality of the plume exhibited by the measurements.

Conclusions

This paper summarized experimental and modeling investigations of PPT plumes. The goal of these investigations is to enhance our understanding of PPT plumes and to provide an advanced predictive ability that will address PPT/spacecraft integration issues. Our experimental investigations started with the plume of the LES 8/9 PPT using single langmuir probes, fast ionization gauge, and a residual gas analyzer. Measurements were restricted to the perpendicular to the electrodes half-plane and covered the region from the centerline to the backflow. Our findings indicate ion speeds of 30 and 60 km/s, a neutral plasmoid expansion that continues for up to 1 ms after the discharge, and the presence of C, F, C_xF_y, and other thruster materials in the plume. Our subsequent plume investigations of a laboratory PPT operating at 5, 20, and 40 J used triple langmuir probes and provided the electron density and temperature

on half-planes perpendicular and parallel to the electrodes. Radial distances varied from 6 to 20 cm from the Teflon surface at polar angles of 10, 20, and 30 deg. Electron density and temperature showed radial and angular variation in the perpendicular to the electrodes plane while they remained uniform in the parallel plane.

Computational modeling of the partially ionized, collisional, and unsteady PPT plume was accomplished by developing a hybrid (particle–fluid) methodology. Ions and neutrals are modeled with a combined DSMC/hybrid-PIC method that includes neutral–neutral, ion–neutral, and ion–electron collisions. The electrons are modeled as a fluid with momentum and energy equations while electric fields are obtained from a charge conservation equation. Modeling results show the expansion of the neutral and ion components of the plume, as well as the generation of charge exchanges ions and neutrals. Overall, numerical results compare well with triple langmuir probe data.

Further experiments are needed to explore the composition and energy distribution in the PPT plume. Measurements in the backflow plane are also essential for assessment of backflow contamination. In addition, coverage of the entire plane is needed to address the PPT plume asymmetry. The conditions at the exit plane of the PPT are also important for plume simulations, as well as understanding the plasmadynamic and gasdynamic acceleration mechanisms in the PPT channel. Future numerical investigations need to be based on a fully three-dimensional model to address the three-dimensional character of the plume. Ionization and recombination mechanisms and other chemical interactions and issues related to current coupling of the plume with the background should also be investigated.

Acknowledgments

This work was funded in part by NASA Grant NAG3-1873. We gratefully acknowledge Fellowship support for Robert Eckman by the Massachusetts Space Grant Consortium. Contributions to this review are based also in the work of Lawrence Byrne and Michael Gagne.

References

[1]Guman, W. J., and Nathanson, D. M., "Pulsed Plasma Microthruster Propulsion System for Synchronous Orbit Satellite," *Journal of Spacecraft and Rockets*, Vol. 7, No. 4, 1970, p. 409.

[2]Brill, Y., Eisner, A., and Osborn, L., "The Flight Application of a Pulsed Plasma Microthruster: The NOVA Satellite," AIAA Paper 82-1956, Nov. 1982.

[3]Myers, R. M., Oleson, S., McGuire, M., Meckel, N., and Cassady, R. J., "Pulsed Plasma Thruster Technology for Small Satellite Missions," NASA CR 198427, Nov. 1995.

[4]Burton, R. L., and Turchi, P. J., "Pulsed Plasma Thruster," *Journal of Propulsion and Power*, Vol. 14, No. 5, 1998, p. 716.

[5]Vondra, R. J., Thomassen, K., and Solbes, A., "Analysis of Solid Teflon Pulsed Plasma Thruster," *Journal of Spacecraft and Rockets*, Vol. 7, No. 12, 1970, pp. 1402–1406.

[6]Thomassen, K. I., and Vondra, R. J., "Exhaust Velocity Studies of a Solid Teflon Pulsed Plasma Thruster," *Journal of Spacecraft and Rockets*, Vol. 9, No. 1, 1972, pp. 61–64.

[7]Thomassen, K. I., and Tong, G., "Interferometric Density Measurements in the Arc of a Pulsed Plasma Thruster," *Journal of Spacecraft and Rockets*, Vol. 10, No. 3, 1973, pp. 163, 164.

[8]Guman, W. J., and Begun, M., "Exhaust Plume Studies of a Pulsed Plasma Thruster," AIAA Paper 78-704, April 1978.

[9]Rudolph, L. K., Harstad, K. G., Pless, L. C., and Jones, R. M., "Plume Characterization of a One-Millipound Solid Teflon Pulsed Plasma Thruster," Air Force Rocket Propulsion Lab. TR-79-60, NASA CR-162786, Sept. 1979.

[10]Hirata, M., and Murakami, H., "Exhaust Gas Analysis of a Pulsed Plasma Engine," AIAA Paper 84-52, May 1984.

[11]Myers, R. M., Arrington, L. A., Pencil, E. J., Carter, J., Heminger, J., and Gatsonis, N. A., "Pulsed Plasma Thruster Contamination," AIAA Paper 96-2729, July 1996.

[12]Eckman, R., Gatsonis, N. A., Myers, R., and Pencil, E., "Experimental Investigation of the LES-8/9 Pulsed Plasma Thruster Plume," 25th International Electric Propulsion Conf., IEPC Rept. 97-126, Aug. 1997.

[13]Markusic, T. E., and Spores, R. A., "Spectroscopic Emission Measurements of a Pulsed Plasma Thruster Plume," AIAA Paper 97-2924, July 1997.

[14]Spanjers, G. G., Malak, J. B., Leiweke, R. J., and Spores, R. A., "Effect of Propellant Temperature in the Pulsed Plasma Thruster," *Journal of Propulsion and Power*, Vol. 14, No. 4, 1998, pp. 545–553.

[15]Eckman, R., "Langmuir Probe Measurements in the Plume of a Pulsed Plasma Thruster," M. S. Thesis, Mechanical Engineering Dept., Worcester Polytechnic Inst., Worcester, MA, Feb. 1999.

[16]Spanjers, G. G., Lotspeich, J. S., McFall, K. A., and Spores, R. A., "Propellant Losses Because of Particulate Emission in a Pulsed Plasma Thruster," *Journal of Propulsion and Power*, Vol. 14, No. 4, 1998, pp. 554–559.

[17]Arrington, L. A., and Haag, T. W., "Multi-Axis Thrust Measurement of the EO-1 PPT," AIAA Paper 99-2290, June 1999.

[18]Arrington, L. A., Marrese, C. M., and Blandino, J. J., "Pulsed Plasma Thruster Plume Study: Symmetry and Impact on Spacecraft Surfaces," AIAA Paper 2000-3262, July 2000.

[19]Eckman, R., Byrne, L., Gatsonis, N. A., and Pencil, E., "Triple Langmuir Probe Measurements in the Plume of a Pulsed Plasma Thruster," *Journal of Propulsion and Power* (to be published).

[20]Gatsonis, N. A., and Yin, X., "Theoretical and Computational Analysis of Pulsed Plasma Thruster Plumes," 25th International Electric Propulsion Conf., IEPC Rept. 97-041, Aug. 1997.

[21]Yin, X., and Gatsonis, N. A., "Numerical Investigation of Pulsed Plasma Thruster Plumes," 25th International Electric Propulsion Conf., IEPC Rept. 97-036, Aug. 1997.

[22]Yin, X., "Axisymmetric Hybrid Numerical Modeling of Pulsed Plasma Thruster Plumes," Ph.D. Dissertation, Mechanical Engineering Dept., Worcester Polytechnic Inst., Worcester, MA, June 1999.

[23]Gagne, M., "Experimental and Numerical Investigation of Gas-Fed PPT Plumes," M.S. Thesis, Mechanical Engineering Dept., Worcester Polytechnic Inst., Worcester, MA, Jan. 2000.

[24]Gatsonis, N. A., and Gagne, M., "Electron Temperature Effects on Pulsed Plasma Thruster Plume Expansion," AIAA Paper 2000-3428, July 2000.

[25]Gatsonis, N. A., and Yin, X., "Hybrid (Particle–Fluid) Modeling of Pulsed Plasma Thruster Plumes," *Journal of Propulsion and Power* (to be published); also AIAA Paper 99-2299, June 1999.

[26]Antropov, N., Gomilka, L., Diakonov, G., Krivonosov, I., Popov, G., and Orlov, M., "Parameters of Plasmoids Injected by PPT," AIAA Paper 97-2921, July 1997.

[27]Chen, S., and Sekiguchi, T., "Instantaneous Direct-Display System of Plasma Parameters by Means of Triple Probe," *Journal of Applied Physics*, Vol. 26, No. 8, 1965, pp. 2363–2375.

[28]Chen, S., "Studies of the Effect on Ion Current on Instantaneous Triple-Probe Measurements," *Journal of Applied Physics*, Vol. 42, No. 1, 1971, pp. 406–412.

[29]Tilley, D. L., Kelly, A. J., and Jahn, R. G., "The Application of the Triple Probe Method to MPD Thruster Plumes," AIAA Paper 90-2667, July 1990.

[30]Bufton, S. A., Burton, R. L., and Krier, H., "Measured Plasma Properties at the Exit Plane of a 1 kW Arcjet," AIAA Paper 95-3066, July 1995.

[31]Gallimore, A. D., Kell, A. J., and Jahn, R. G., "Anode Power Deposition in Quasi-Steady MPD Thusters," AIAA Paper 90-2668, 1990.

[32]Burton, R., and Bushman, S., "Probe Measurements in a Coaxial Gasdynamic PPT," AIAA Paper 99-2288, July 1999.

[33]Bird, G. A., *Molecular Gas Dynamics and the Direct Simulation of Gas Flows*, Clarendon, Oxford, England, U.K., 1994.

[34]Jones, M. E., Lemons, D. S., Mason, R. J., Thomas, V. A., and Winske, D., "A Grid-Based Coulomb Method for PIC Codes," *Journal of Computational Physics*, Vol. 123, 1996, pp. 169–181.

[35]Samanta Roy, R. I., Hastings, D. E., and Gatsonis, G. A., "Ion-Thruster Plume Modeling For Backflow Contamination," *Journal of Spacecraft and Rockets*, Vol. 33, No. 4, 1996, pp. 525–534.

[36]Gatsonis, N. A., Yin, and X., Buzby, J., "Particle Simulation of Partially Ionized Hydrogen Plumes," *Rarefied Gas Dynamics*, edited by C. Shen, Peking Univ. Press, Beijing, 1997, pp. 561–566.

[37]Oh, D., "Modeling of Stationary Plasma Thruster-100 Thruster Plumes and Implications for Satellite Design," *Journal of Propulsion and Power*, Vol. 15, No. 2, 1999, pp. 345–357.

[38]VanGilder, D. B., Boyd, I. D., and Keidar, M., "Particle Simulations of a Hall Thruster Plume," *Journal of Spacecraft and Rockets*, Vol. 37, No. 1, 2000, pp. 129–136.

[39]Boyd, I. D., Keidar, M., and McKeon, W., "Modeling of a Pulsed Plasma Thruster From Plasma Generation to Plume Far Field," *Journal of Spacecraft and Rockets*, Vol. 37, No. 3, 2000, pp. 399–407.

[40]Turchi, P. J., and Mikellides, P. G., "Modeling of Ablation-Fed Pulsed Plasma Thrusters," AIAA Paper 95-2915, July 1995.

I. D. Boyd
Associate Editor